

Conditional probability density functional theory for solids

Peiwei You,^{1,*} Ryan Pederson,² Kieron Burke,^{2,†} and E. K. U. Gross^{1,3,‡}

¹*Fritz Haber Center for Molecular Dynamics, Institute of Chemistry, The Hebrew University of Jerusalem, Jerusalem 91904, Israel*

²*Departments of Physics and Astronomy and of Chemistry, University of California, Irvine, California 92697, USA*

³*Quantum Dynamics Laboratory, Tsientang Institute of Advanced Study, Hangzhou, Zhejiang, 310024, P.R. China*

A recently developed approach, conditional probability density functional theory (CP-DFT), yields direct access to the exchange-correlation hole of a system, an important correlation function that is not available from any standard DFT calculation. We present the first results for extended materials with periodic boundary conditions. We demonstrate that CP-DFT works on weakly correlated materials (Na, Si). When applied to the prototypical Kagome material CsV_3Sb_5 , we find d -orbital correlations that are not captured by standard DFT. Such distribution leads to a positive finding probability between two separated electrons and an enhanced charge density wave signal, suggesting a useful approach for strongly correlated systems.

Kohn-Sham (KS) density functional theory (DFT) is the cornerstone for modeling complex chemical and material systems [1]. Its widespread utility is due to the development of exchange-correlation (XC) functionals that, despite being approximations, reliably predict ground-state energies and structural properties [2]. While these functionals are often designed to satisfy exact physical conditions [3] and yield accurate energetics, they typically rely on a simplified mapping that obscures the intricate, real-space electron correlations that are central to modern condensed matter physics.

The primary limitation involves the representation of the pair density, which characterizes the probability of finding an electron at a specific coordinate relative to a reference electron at another position [4]. This quantity encompasses the XC hole, the depletion of electron density surrounding a reference electron arising from Pauli exclusion and Coulomb repulsion. In conventional KS-DFT, the complex spatial topology of this hole is typically reduced to simplified "on-top" or spherically averaged approximations [5–8]. While these models are effective for determining total energies, they purposely obscure the pointwise fine structure of the electronic environment [9], in favor of system- and spherical-averages that yield XC energies. This loss of spatial resolution could be critical because detailed correlation structures can be the fundamental physical drivers of emergent phenomena. In Mott insulators such as NiO and MnO, for example, strong on-site Coulomb repulsion drives the formation of the Mott gap [10, 11]. While charge density wave (CDW) formation is often attributed to momentum-dependent electron-phonon coupling and Fermi surface nesting [12], an emerging perspective highlights the potential involvement of electron correlations in CDW and even pair density wave orders in Kagome metals upon entering the superconducting state [13–15]. Determining the pair density to uncover the nature of these correlations in such electronic orders represents an important step toward a deeper understanding of correlated quantum matter.

Recently, conditional probability (CP) density functional theory has been proposed [16] as an alternative to KS-DFT, especially for systems with strong correlations [17]. CP-DFT is a formally exact framework to directly calculate pointwise pair densities, offering a way to capture the correlated structure of the electronic environment [16]. In CP-DFT, the pair density itself is directly calculated by a sequence of Kohn-Sham-like calculations at every real space position \mathbf{r} in the system. These calculations employ an approximate CP-KS potential to yield the CP density, $n_{\mathbf{r}}(\mathbf{r}')$, the conditional probability of finding an electron at \mathbf{r}' given an electron at \mathbf{r} , and thus the pair density $P(\mathbf{r}, \mathbf{r}') = n(\mathbf{r})n_{\mathbf{r}}(\mathbf{r}')$, where $n(\mathbf{r})$ is the ground state electron density. Since the pair density determines the interaction and total energies, CP-DFT bypasses the need to capture strong correlation effects in an explicit density functional. Within this paradigm, CP-DFT correctly dissociates H_2 and arbitrary-length H chains, a classic example where KS-DFT XC functionals notoriously fail [16, 17].

While previous applications of CP-DFT were limited to atomic and molecular systems [17] and simple models [18] where standard KS-DFT typically fails, the present work extends CP-DFT to periodic systems and establishes a comprehensive and highly scalable framework for extended solid-state materials. By incorporating periodic boundary conditions and leveraging massive parallelization, we render the direct calculation of the pointwise pair density computationally tractable for realistic crystalline systems of interest.

We implement this first-principles approach by solving the CP-KS equations self-consistently for each reference point across the periodic cell. We validate the method using both isolated (Helium) and periodic (Sodium, Silicon) systems, demonstrating our ability to resolve the pointwise structure of the XC hole in a crystalline environment. As a prototype for complex quantum matter, we apply this framework to the Kagome metal

CsV₃Sb₅. Our results reveal spatial modulations of the pair density and d -orbital correlated structures that are missed in averaged density functional approximations. These correlations lead to an enhanced charge density wave signal and improved density of states near the Fermi level, illustrating how the direct calculation of the pair density provides a deeper understanding of the electronic structure in strongly correlated materials.

Within the adiabatic connection formalism, we consider an N -electron system subject to a scaled Coulomb repulsion, characterized by a non-negative coupling strength λ , such that the ground-state electronic density $n(\mathbf{r})$ remains fixed [19, 20]. The λ -dependent pair density can be expressed as $P^\lambda(\mathbf{r}, \mathbf{r}') = n(\mathbf{r})n_{\mathbf{r}}^\lambda(\mathbf{r}')$, where $n_{\mathbf{r}}^\lambda(\mathbf{r}')$ is the CP density. This term represents the probability of finding an electron at \mathbf{r}' given a reference electron located at \mathbf{r} and a Coulomb repulsion scaled by λ . CP-DFT provides a framework to determine this pointwise λ -dependent density by self-consistently solving the CP-KS equations for an $(N - 1)$ -electron system with an effective potential $v_{s,\mathbf{r}}^\lambda(\mathbf{r}')$:

$$v_{s,\mathbf{r}}^\lambda(\mathbf{r}') = v_s[n](\mathbf{r}') - v_{\text{HXC}}^\lambda[n](\mathbf{r}') + \Delta v_{\mathbf{r}}^\lambda(\mathbf{r}') + v_{\text{HXC}}^\lambda[n_{\mathbf{r}}^\lambda](\mathbf{r}'), \quad (1)$$

where $v_s[n](\mathbf{r}')$ is the standard KS potential for the ground-state density. The terms $v_{\text{HXC}}^\lambda[n](\mathbf{r}')$ and $v_{\text{HXC}}^\lambda[n_{\mathbf{r}}^\lambda](\mathbf{r}')$ are the λ -dependent Hartree and XC components evaluated on the ground-state and CP densities, respectively, while $\Delta v_{\mathbf{r}}^\lambda(\mathbf{r}')$ serves as the CP correction potential [17] (Supplementary Note 1 [21]). While CP-DFT is formally exact—yielding the exact CP density given the exact XC and CP correction potentials—these terms must be approximated in practical applications. We employ traditional KS-DFT XC functionals to obtain the necessary XC potentials, specifically relying on the Perdew–Burke–Ernzerhof (PBE) generalized gradient approximation (GGA) [22] throughout this study. PBE satisfies essential exact conditions and is computationally more efficient than modern meta-GGA variants [23]. To approximate the CP correction potential, we utilize a variant of the local blue electron approach [16, 17]. This classically inspired method has recently been shown to satisfy several key exact conditions within CP-DFT [6, 17].

Computationally, the CP-KS equations can be solved using standard KS-DFT methodology. We employ the SIESTA code [24, 25], using its numerical atomic basis set to handle large systems with extensive real-space grids, and pseudopotentials to avoid calculating core electrons. In this way, we directly obtain the pseudo-density in CP-DFT following the process in Fig. 1. The λ -dependent Hartree-XC potentials with respect to KS and CP density are calculated via uniform coordinate scaling relations [26] (Supplementary Note 1 [21]). However, unlike standard KS-DFT, the CP-KS framework requires solving

these equations independently across a dense spatial grid of reference points and a mesh of coupling strengths λ . Fortunately, these requirements are highly amenable to massive parallelization.

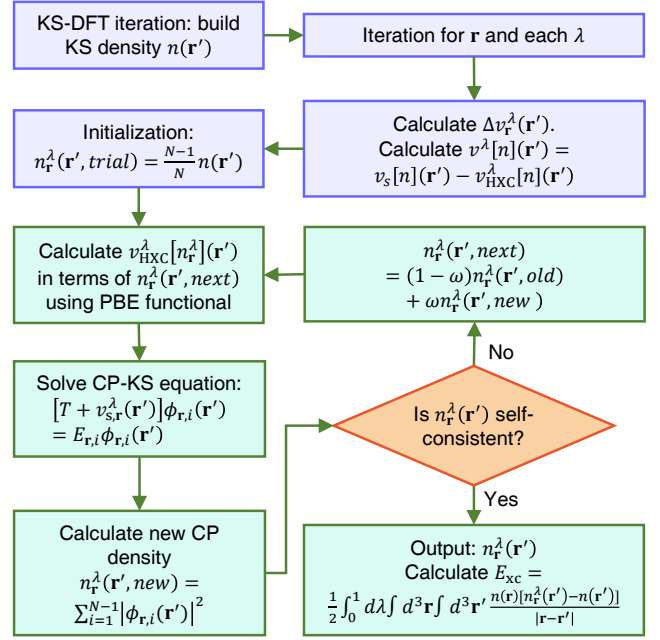


FIG. 1. Schematic flowchart of the CP-DFT framework using the first-principles approach. The standard KS-DFT is performed firstly to gain the KS density and KS potential. To obtain the CP density, electronic iterations are performed for reference points and each coupling strength. Here we use the PBE functional with respect to KS and CP density to calculate the λ -dependent XC potential.

We first verify our first-principles approach on three representative systems: a periodic sodium metal, an isolated helium atom, and bulk silicon. In the exchange-only limit ($\lambda = 0$), the definition of CP density dictates that $n_{\mathbf{r}}^\lambda(\mathbf{r}')$ evaluates to half the ground-state density $n(\mathbf{r}')$ at the reference point. We quantitatively confirm this relation for both two-electron systems sodium metal (Fig. 2a-b) and the helium atom (Supplementary Fig. S1-2 [21]). By setting the reference point at the center and corner of the Na cell, we visualize the pointwise exchange-only hole ($n_{\text{XC}}^{\lambda=0}$), the full XC hole ($n_{\text{XC}}^{\lambda=1}$), and the correlation hole ($n_{\text{XC}}^{\lambda=1} - n_{\text{XC}}^{\lambda=0}$) on a two-dimensional (2D) surface (Supplementary Fig. S3-4 [21]). The exchange hole closely mirrors the shape of the KS density, while the correlation hole reshapes the profile due to Coulomb repulsion, illustrating a generic picture for conventional systems [27]. As shown in Supplementary Fig. S5 [21], the XC holes are featureless and similar to those obtained from local density approximation (LDA). In helium, the CP density ($\lambda = 1$) is suppressed along the bond but enhanced near 0.5 Å relative to the exchange limit. For bulk silicon (Supplementary Fig. S6 [21]), the XC holes reveal

strong repulsion within bonding regions. The XC energies from CP-DFT, integrated over all real-space points and λ , agree closely with KS-PBE values: -8.4 eV vs. -8.16 eV for Na, -28.30 eV vs. -28.11 eV for He, and -65.47 eV vs. -64.89 eV for Si. These results demonstrate CP-DFT yields energies comparable to its PBE counterpart for weakly correlated systems.

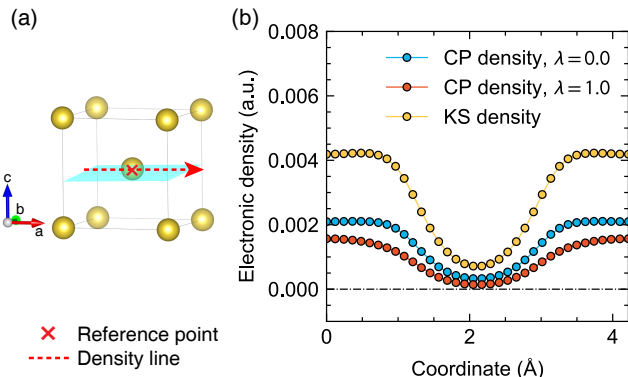


FIG. 2. (a-b) In the metallic Sodium system, we set the reference point in the center of the box to show the CP density linecut for $\lambda = 0.0$ and $\lambda = 1.0$ obtained from CP-DFT, and the KS density from KS-DFT. The linecut is denoted in (a) across the center point at the half of the simulation box.

Next, we apply CP-DFT to a more complex periodic system: the Kagome metal CsV_3Sb_5 . This compound serves as an excellent proving ground for studying non-trivial band topology [28], CDW, and superconductivity [29, 30]. At room temperature, CsV_3Sb_5 maintains a hexagonal structure comprising a V-atom Kagome layer sandwiched by honeycomb layers of Sb atoms (Fig. 3a). Its electronic band structure features van Hove singularities and Dirac points near the Fermi surface. Upon cooling, CsV_3Sb_5 undergoes a CDW transition at 80–100 K, followed by a superconducting transition below ~ 2.8 K [13]. The system exhibits 2×2 CDW phases characterized by “star of David” structural distortions from the pristine Kagome lattice, as well as an inverse displacement phase. Theoretical work suggests the most stable configuration favors this inverse star of David (ISD) deformation [14], where the V atoms form the distorted structure shown in Fig. 3a. To account for long-range electronic correlations, we employ a $4 \times 4 \times 1$ supercell, sampling the Brillouin zone with a $2 \times 2 \times 2$ K-point mesh (detailed in Supplementary Note 2 [21]). Our calculations utilize supercell lattice constants of $a = 21.98$ Å and $c = 9.88$ Å, an energy cutoff of 600 Ry, and 12 million real-space mesh points. For such a large system, the computational cost is prohibitively high, making it impractical to calculate every point to extract the XC energy. The convergence criterion for the Hamiltonian matrix in self-consistent calculations is set to 1×10^{-4} Ry.

In Fig. 3b, we present the pointwise CP density at

the V-Sb layer exhibiting the ISD distortion. Given that paired electrons are observed near the V atoms [13], we deliberately position the reference electron within a high-density region near a Vanadium atom (specifically at $x = 2.083 a_0$, $y = 2.083 a_0$, beyond the core) to explicitly probe the localized electron interactions. As confirmed by the projected and local density of states (Supplementary Fig. S7 [21]), the total electronic density at this coordinate is overwhelmingly dominated by V $3d$ orbitals, with negligible contribution from Sb states. Consequently, the resulting CP density distribution serves as a direct, real-space map of the V $3d$ local bonding structure. While standard KS-DFT depicts these orbitals as pristine, symmetric high-density clouds, the explicit Coulomb repulsion introduced in CP-DFT drastically reshapes this immediate environment. Specifically, the CP density flattens near the reference electron, and the characteristic symmetry of the $3d$ orbital is starkly disrupted or “broken” (Fig. 3b). To further illustrate this local depletion, we plot a density linecut along the a -axis in Fig. 3c. Although the majority of the CP density remains concentrated around the V atoms, it is significantly repelled from the reference coordinate, capturing the precise, real-space topology of the electron-electron interaction.

The fine structure of the CP density offers deep insights into the intrinsic properties of these materials. Along the density linecut (Fig. 3b), we analyze the fine-structure differences manifested in the XC hole (Fig. 4). For comparison, we calculate the LDA XC hole using the Perdew–Wang 92 parameterization [31] (Supplementary Note 3 and Fig. S11 [21]), which inherently exhibits a monotonic and spherical profile. All holes are weighted and normalized by their respective KS densities. As the reference points are scanned left to right across the d -orbital density peaks ($1.917 a_0$ to $2.167 a_0$), the XC holes initially intensify and then diminish (Fig. 4a). Notably, for each reference point, the CP-DFT XC hole exhibits a main peak adjacent to the reference point and a secondary shoulder or peak near a neighboring d -orbital KS density peak. In contrast, the LDA hole displays only a single featureless peak. These distinctions are further emphasized in the averaged XC hole, calculated over 32 reference points ($1.61 a_0$ to $2.47 a_0$). The CP-DFT XC hole is heavily concentrated in the on-top region (near $2.1 a_0$), whereas the LDA result remains broad and diffuse. This double-peak structure between $1.9 a_0$ and $2.1 a_0$ indicates pronounced repulsion within the high-density region, revealing local deformations of the V $3d$ electrons. Interestingly, the Coulomb interaction induces small positive density waves near the V atom (at both $1 a_0$ and $3 a_0$), manifesting as an enhanced probability of finding two electrons at a spatial separation of $\sim 1 a_0$. These positive waves are highlighted in the inset figures and are more significant in the scaled XC holes shown in Supplementary Fig. S8 [21]. These alternating positive and negative

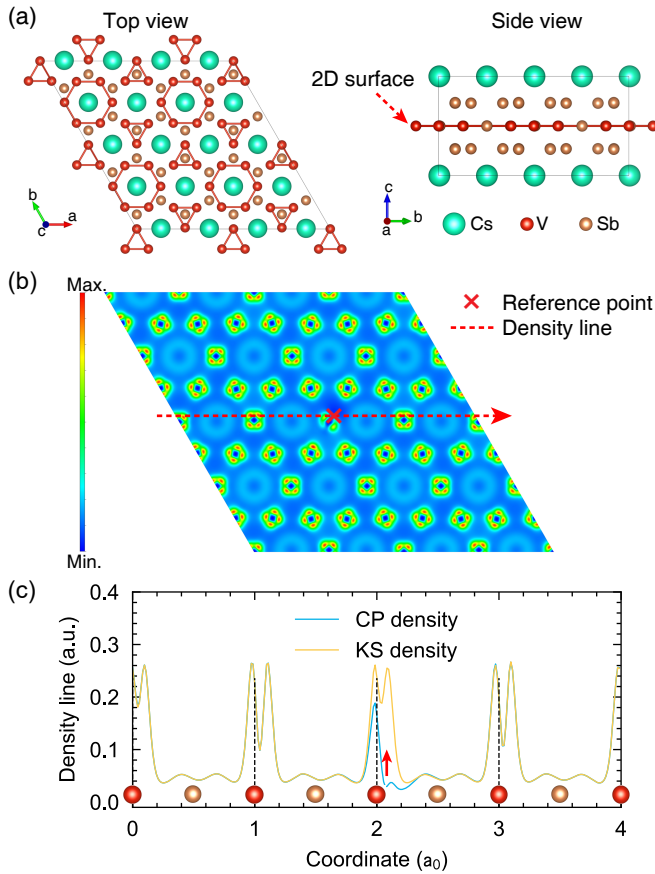


FIG. 3. (a) Top and side view for atomic structure of CsV_3Sb_5 , with ISD. Totally 144 atoms are involved in this $4 \times 4 \times 1$ supercell. The green, red and brown balls indicate the Cs, V and Sb atoms, respectively. (b) The simulated 4×4 CP density in the 2D surface shown in (a), which is also the value of pair density scaled by $1/n(\mathbf{r})$ at the reference point. Red cross displays the reference point near the center. (c) The CP density from CP-DFT and the conventional density from KS-DFT, along the specific line shown in (b). Here a_0 denotes the single cell lattice constant.

peaks are responsible for the enhanced CDW signal, directly contributing to the amplification and reduction of the CDW amplitude. Such seemingly counterintuitive feature—where strong repulsion coincides with an enhanced probability of finding two electrons at a finite separation—suggests the emergence of non-local correlation patterns within the pair density. The fundamental difference is starkly visible in the Fourier transform of the density linecut (Fig. 4b). While the LDA result decays rapidly in momentum space, the CP-DFT results exhibit prominent peaks between $5 Q_{\text{Bragg}}$ and $8 Q_{\text{Bragg}}$ arising from the double-peak structure, along with a small enhancement at $Q=1/2 Q_{\text{Bragg}}$. The high-frequency peaks imply the presence of short-range orders that are entirely absent in conventional XC functionals, underscoring the profound impact of complex electron-electron interactions on the Kagome lattice.

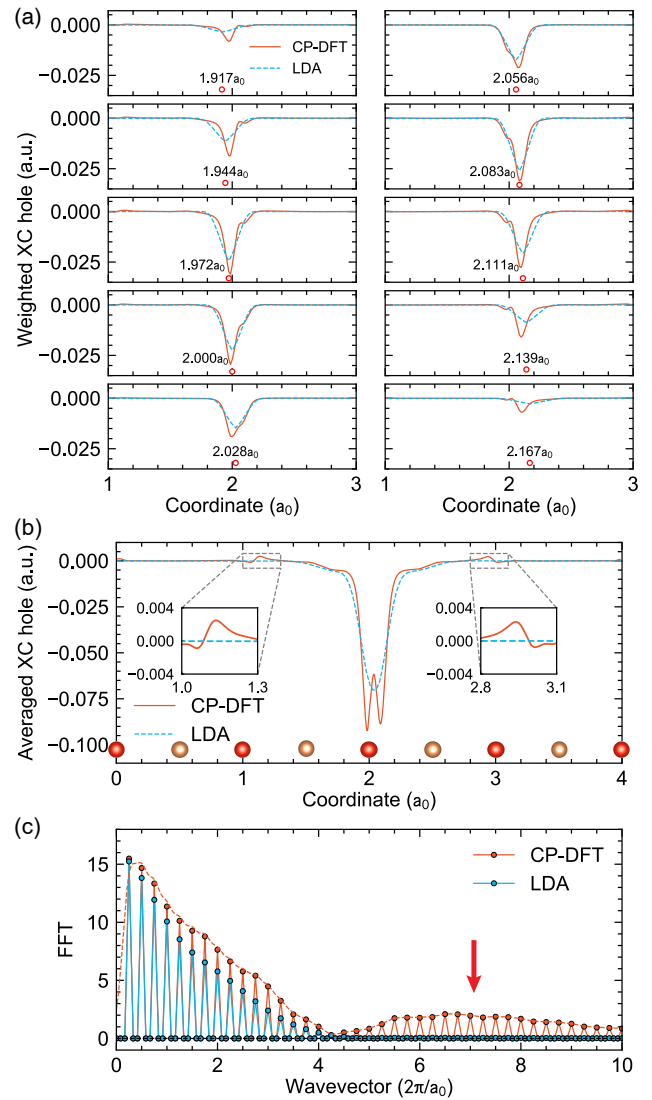


FIG. 4. (a) The XC holes ($\lambda = 1.0$) and LDA holes at 10 reference points ranging from $1.917 a_0$ to $2.167 a_0$ in steps of $0.028 a_0$. The holes are weighted and normalized by the respective KS densities. Red circles and texts display the reference positions on the a axis while $y=2.083 a_0$. (b) The XC hole from both CP-DFT and LDA along the a axis in the supercell, averaged over 32 reference points in $1.61 a_0 \sim 2.47 a_0$ (with an interval of $0.028 a_0$). The density linecut is shown in Fig. 3(b). (c) Fourier transform spectrum for the averaged XC hole linecut in (b). The dashed line indicates an approximate envelope of component peaks in CP-DFT. The wavevector unit is $Q_{\text{Bragg}} = 2\pi/a_0$.

Finally, we examine how these explicit electron-electron interactions influence the electronic structure in momentum space. In CP-DFT, fixing a reference electron locally breaks the pristine translational symmetry of the lattice, necessitating a supercell treatment. By diagonalizing the CP Hamiltonian within the supercell Brillouin zone, we obtain the eigenstates for the remaining $N - 1$ electrons interacting with the fixed reference charge.

To analyze these states in the context of the pristine lattice, we project these supercell eigenfunctions back onto the primitive unit cell. This unfolding procedure yields the spectral weight in the first Brillouin zone, representing the momentum-resolved density of states (Supplementary Fig. S9 [21]). To isolate the impact of explicit electron correlations on this electronic structure, we calculate the difference in spectral weight (Fig. 5). By subtracting the exchange-only baseline ($\lambda = 0$) from the fully interacting system ($\lambda = 1$), we reveal the specific energetic shifts that are fundamentally driven by electron correlation. This subtraction visually maps these correlation-induced changes across the Brillouin zone: it highlights where electron states are depleted from their original positions (indicated by negative, blue regions) and where they are shifted to (indicated by positive, red regions). Examining these correlation-driven shifts, we find that at the M point, the upper mixture-type van Hove singularity (vHS) at 0.1 eV [32] remains unperturbed. This preserves the band dispersion’s charge order gap, implying that electron-electron correlation does not destroy the experimentally observed charge order. More importantly, CP-DFT predicts a 20–40 meV downward shift in both the energy and spectral weight of the vHS band near the Fermi level. This finding suggests that correlation-driven band shifts—similar in spirit to those recently observed in CsCr₃Sb₅ system, where standard DFT fails without phenomenological correlation [33, 34]. Such a prediction emerges self-consistently from *d*-orbital correlations and awaits further experimental verification. Unlike Mott on-site repulsion, this downward shift is an indication of effective attraction between spatially separated electrons. Far from the reference point (Supplementary Fig. S10 [21]), the negative potential arising from the XC hole competes with the direct Coulomb repulsion. The combined effect yields a net attractive tendency, emerging from the interplay between correlation-induced screening and the bare Coulomb interaction. These spectral changes strongly suggest that electron-electron interactions—properly captured by the correlated pair density—meaningfully influence the low-energy electronic landscape relevant to superconductivity.

We have implemented CP-DFT for periodic solids and demonstrated its capability to compute the point-wise pair density and XC hole in crystalline materials. The method extends the formally exact CP framework to extended systems by solving self-consistent conditional Kohn–Sham equations at fixed reference positions. Benchmark calculations for He, Na and Si confirm the correct exchange limit and yield close XC energies to standard KS results. In the Kagome metal CsV₃Sb₅, CP-DFT reveals correlated structures with local bonding information of *3d* orbitals not captured by averaged density approximations. These correlation-induced modulations show a small enhanced amplitude of CDW, providing

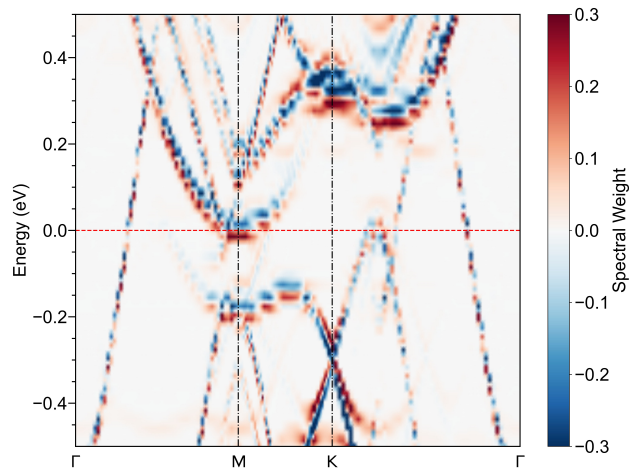


FIG. 5. Difference in spectral weight between $\lambda = 1.0$ and $\lambda = 0.0$ along $\Gamma - M - K - \Gamma$ high-symmetry path. The Fermi level is indicated by the red dashed line. The reference point is located at $x = 2.083 a_0, y = 2.083 a_0$ shown in Fig. 3.

a real-space view of how electron-electron interactions reshape density correlations in a topological metal. By providing access to the full pair density in solids within a first-principles framework, CP-DFT opens a route to analyzing the real-space correlation patterns that underlie electronic instabilities and ordering phenomena beyond conventional energy-based density functional approaches. This work establishes feasibility for extended materials and lays the groundwork for future studies linking real-space pair correlations to collective electronic phases, such as superconductivity or charge order.

E.K.U. Gross acknowledge financial support from the Fondation de l’Ecole Polytechnique within the Gaspard Monge programme. K. Burke is supported by NSF grant DMR-2427903. P. You thanks Sheng Meng for discussion.

* peiwei.you@mail.huji.ac.il

† kieron@uci.edu

‡ eberhard.gross@mail.huji.ac.il

- [1] R. O. Jones, Density functional theory: Its origins, rise to prominence, and future, *Rev. Mod. Phys.* **87**, 897 (2015).
- [2] K. Lejaeghere, V. V. Speybroeck, G. V. Oost, and S. Cottenier, Error estimates for solid-state density-functional theory predictions: An overview by means of the ground-state elemental crystals, *Critical Reviews in Solid State and Materials Sciences* **39**, 1 (2014).
- [3] A. D. Kaplan, M. Levy, and J. P. Perdew, The predictive power of exact constraints and appropriate norms in density functional theory, *Annual Review of Physical Chemistry* **74**, 193 (2023).
- [4] K. Burke and J. P. Perdew, Real-space analysis of the exchange-correlation energy, *International Journal of Quantum Chemistry* **56**, 199 (1995).

- [5] J. P. Perdew, A. Savin, and K. Burke, Escaping the symmetry dilemma through a pair-density interpretation of spin-density functional theory, *Phys. Rev. A* **51**, 4531 (1995).
- [6] P. Gori-Giorgi and A. Savin, Simple model for the spherically and system-averaged pair density: Results for two-electron atoms, *Phys. Rev. A* **71**, 032513 (2005).
- [7] P. Gori-Giorgi and A. Savin, Kohn-sham calculations combined with an average pair-density functional theory, *Int. J. Mod. Phys. B* **21**, 2449 (2007).
- [8] G. Li Manni, R. K. Carlson, S. Luo, D. Ma, J. Olsen, D. G. Truhlar, and L. Gagliardi, Multiconfiguration pair-density functional theory, *J. Chem. Theory Comput.* **10**, 3669 (2014).
- [9] R. O. Jones and O. Gunnarsson, The density functional formalism, its applications and prospects, *Rev. Mod. Phys.* **61**, 689 (1989).
- [10] L. A. Agapito, S. Curtarolo, and M. Buongiorno Nardelli, Reformulation of DFT+U as a pseudohybrid hubbard density functional for accelerated materials discovery, *Phys. Rev. X* **5**, 011006 (2015).
- [11] S. Sharma, J. K. Dewhurst, S. Shallcross, and E. K. U. Gross, Spectral density and metal-insulator phase transition in mott insulators within reduced density matrix functional theory, *Phys. Rev. Lett.* **110**, 116403 (2013).
- [12] X. Zhu, Y. Cao, J. Zhang, E. W. Plummer, and J. Guo, Classification of charge density waves based on their nature, *Proc. Natl. Acad. Sci. U.S.A.* **112**, 2367 (2015).
- [13] H. Chen, H. Yang, B. Hu, Z. Zhao, J. Yuan, Y. Xing, G. Qian, Z. Huang, G. Li, Y. Ye, S. Ma, S. Ni, H. Zhang, Q. Yin, C. Gong, Z. Tu, H. Lei, H. Tan, S. Zhou, C. Shen, X. Dong, B. Yan, Z. Wang, and H. J. Gao, Roton pair density wave in a strong-coupling kagome superconductor, *Nature* **599**, 222 (2021).
- [14] H. Tan, Y. Liu, Z. Wang, and B. Yan, Charge density waves and electronic properties of superconducting kagome metals, *Phys. Rev. Lett.* **127**, 046401 (2021).
- [15] B. Song, T. Ying, X. Wu, W. Xia, Q. Yin, Q. Zhang, Y. Song, X. Yang, J. Guo, L. Gu, X. Chen, J. Hu, A. P. Schnyder, H. Lei, Y. Guo, and S. Li, Anomalous enhancement of charge density wave in kagome superconductor CsV₃Sb₅ approaching the 2d limit, *Nat. Commun.* **14**, 2492 (2023).
- [16] R. J. McCarty, D. Perchak, R. Pederson, R. Evans, Y. Qiu, S. R. White, and K. Burke, Bypassing the energy functional in density functional theory: Direct calculation of electronic energies from conditional probability densities, *Phys. Rev. Lett.* **125**, 266401 (2020).
- [17] R. Pederson, J. Chen, S. R. White, and K. Burke, Conditional probability density functional theory, *Phys. Rev. B* **105**, 245138 (2022).
- [18] D. Perchak, R. J. McCarty, and K. Burke, Correlation energy of the uniform electron gas determined by ground-state conditional probability density functional theory, *Phys. Rev. B* **105**, 165143 (2022).
- [19] D. Langreth and J. Perdew, The exchange-correlation energy of a metallic surface, *Solid State Communications* **17**, 1425 (1975).
- [20] C. Fiolhais, F. Nogueira, and M. A. L. Marques, *A primer in density functional theory* (Springer Science & Business Media, 2003).
- [21] See supplemental material which includes detailed additional data, and computational methods of first principle simulation.
- [22] J. P. Perdew, K. Burke, and M. Ernzerhof, Generalized gradient approximation made simple, *Phys. Rev. Lett.* **77**, 3865 (1996).
- [23] J. Sun, A. Ruzsinszky, and J. P. Perdew, Strongly constrained and appropriately normed semilocal density functional, *Phys. Rev. Lett.* **115**, 036402 (2015).
- [24] J. M. Soler, E. Artacho, J. D. Gale, A. García, J. Junquera, P. Ordejón, and D. Sánchez-Portal, The siesta method for ab initio order-n materials simulation, *J. Phys.: Condens. Matter* **14**, 2745 (2002).
- [25] A. Garcia, N. Papior, A. Akhtar, E. Artacho, V. Blum, E. Bosoni, P. Brandimarte, M. Brandbyge, J. I. Cerda, F. Corsetti, R. Cuadrado, V. Dikan, J. Ferrer, J. Gale, P. Garcia-Fernandez, V. M. Garcia-Suarez, S. Garcia, G. Huhs, R. Illera, R. Korytar, P. Koval, I. Lebedeva, L. Lin, P. Lopez-Tarifa, S. G. Mayo, P. Mohr, P. Ordejón, A. Postnikov, Y. Pouillon, M. Pruneda, R. Robles, D. Sanchez-Portal, J. M. Soler, R. Ullah, V. W. Yu, and J. Junquera, Siesta: Recent developments and applications, *J. Chem. Phys.* **152**, 204108 (2020).
- [26] A. Görling and M. Levy, Correlation-energy functional and its high-density limit obtained from a coupling-constant perturbation expansion, *Phys. Rev. B* **47**, 13105 (1993).
- [27] K. Burke, J. P. Perdew, and M. Ernzerhof, Why semilocal functionals work: Accuracy of the on-top pair density and importance of system averaging, *The Journal of Chemical Physics* **109**, 3760 (1998).
- [28] B. R. Ortiz, S. M. L. Teicher, Y. Hu, J. L. Zuo, P. M. Sarte, E. C. Schueller, A. M. M. Abeykoon, M. J. Krogstad, S. Rosenkranz, R. Osborn, R. Seshadri, L. Balents, J. He, and S. D. Wilson, CsV₃Sb₅: A Z₂ topological kagome metal with a superconducting ground state, *Phys. Rev. Lett.* **125**, 247002 (2020).
- [29] Z. Liang, X. Hou, F. Zhang, W. Ma, P. Wu, Z. Zhang, F. Yu, J. J. Ying, K. Jiang, L. Shan, Z. Wang, and X. H. Chen, Three-dimensional charge density wave and surface-dependent vortex-core states in a kagome superconductor CsV₃Sb₅, *Phys. Rev. X* **11**, 031026 (2021).
- [30] H. Zhao, H. Li, B. R. Ortiz, S. M. L. Teicher, T. Park, M. Ye, Z. Wang, L. Balents, S. D. Wilson, and I. Zeljkovic, Cascade of correlated electron states in the kagome superconductor CsV₃Sb₅, *Nature* **599**, 216 (2021).
- [31] J. P. Perdew and Y. Wang, Pair-distribution function and its coupling-constant average for the spin-polarized electron gas, *Phys. Rev. B* **46**, 12947 (1992).
- [32] M. Kang, S. Fang, J.-K. Kim, B. R. Ortiz, S. H. Ryu, J. Kim, J. Yoo, G. Sangiovanni, D. Di Sante, B.-G. Park, C. Jozwiak, A. Bostwick, E. Rotenberg, E. Kaxiras, S. D. Wilson, J.-H. Park, and R. Comin, Twofold van hove singularity and origin of charge order in topological kagome superconductor CsV₃Sb₅, *Nat. Phys.* **18**, 301 (2022).
- [33] Z. Wang, Y. Guo, H.-Y. Huang, F. Xie, *et al.*, Spin excitations and flat electronic bands in a cr-based kagome superconductor, *Nat. Commun.* **16**, 7573 (2025).
- [34] F. Xie, Y. Fang, Y. Li, Y. Huang, L. Chen, C. Setty, S. Sur, B. Yakobson, R. Valentí, and Q. Si, Electron correlations in the kagome flat band metal cscr₃sb₅, *Phys. Rev. Res.* **7**, L022061 (2025).